Electron Transfer and Electron Exchange between [Cp*(dppe)Fe]$^{n+}$ (n = 0, 1) Building Blocks Mediated by the 9,10-Bis(ethynyl)anthracene Bridge

Frédéric de Montigny,[†] Gilles Argouarch,[†] Karine Costuas,[‡] Jean-François Halet,*[,‡] Thierry Roisnel,[‡] Loic Toupet,[§] and Claude Lapinte*[,†]

Institut de Chimie de Rennes, Organométalliques et Catalyse, UMR CNRS 6509, Laboratoire de Chimie du Solide et Inorganique Moléculaire, UMR CNRS 6511, and Groupe Matière Condensée et Matériaux, UMR CNRS 6626, Université de Rennes 1, 35042 Rennes, France

Received May 20, 2005

A novel bis(iron) alkynyl-bridged complex, Cp*(dppe)Fe(C≡C-9,10-ant-C≡C)Fe(dppe)Cp*, **10** (ant = anthracene), and its oxidized forms, **10**·PF_6, **10**·TCNQ, and **10**·$2PF_6$, were synthesized and characterized by X-ray crystal structures. The cyclic voltammogram of **10** shows two well-reversible redox couples at −0.40 and −0.04 V (vs SCE) and a third redox process close to the solvent edge. Density-functional theory (DFT) calculations carried out on the substituted model complex (η^5-C_5H_5)(η^2-dpe)Fe−C≡C-9,10-ant-C≡C−Fe(η^2-dpe)(η^5-C_5H_5), **10-H** (dpe = H_2P−$(CH_2)_2$−PH_2), suggest that the HOMO, which is depopulated upon oxidation, has a dominant anthracene character. The ^{1}H NMR and the magnetic susceptibility measurements indicate that the complex **10**·$2PF_6$ is diamagnetic, in contrast with that of its congeners of the bis(iron) series, which do not contain the anthracene fragment in the bridge. Experimental measurements and DFT calculations reveal a large energy gap between the singlet ground state and the triplet excited state (ΔE_{ST}(exp) < −1200 cm^{-1}). Mössbauer spectroscopy reveals that the two iron centers are spectroscopically equivalent for the three oxidation states. The parameters found for **10**·$2PF_6$ are not typical of an iron(III) center, but rather characteristic of iron(II). The spectrum of **10**·TCNQ is in accord with a detrapped mixed-valence (MV) electronic structure with a large contribution of the delocalized unpaired electron on the carbon bridge. In addition, Mössbauer and UV−vis data and DFT calculations indicate also that the electronic structure of the MV complex is much closer to the dication **10**·$2PF_6$ than the parent complex **10**. The analysis of the NIR absorption band allows the determination of a large electronic coupling parameter, as expected for a class III MV complex (V_{ab} = 2180 cm^{-1}). Taken as a whole, the experimental and theoretical data emphasize the specific role of the anthracene fragment inserted in the carbon bridge, which allows good electronic communication between the iron centers, but significantly contributes to the displacement of the spin density from the metal centers onto the α and β sp carbon atoms in the vicinity of the metal and the *ipso* carbon of the anthracene.

Introduction

The development of organic or organometallic supermolecules with tailor-made properties such as recognition, switching ability, and long-range electronic, magnetic, and charge communication appears as a prerequisite to the development of molecular electronics.[1−3] Efficient electron conveyors have been elaborated by linking two redox-active organometallic building blocks with polyynediyl fragments.[4−6] The chemical and physical properties of these fascinating molecules can be switched by selective and reversible oxidation/reduction of the termini.[7−10] Spectroscopic investigations and DFT calculations indicate that the bonding of the bridges can apparently be switched from a polyynediyl structure into a cumulenic structure by two successive one-electron oxidations.[10,11] Meanwhile a variety of binuclear compounds with carbon chains consisting of as many as 20 atoms have received considerable attention,[12] and the tetracarbon species $LnMC_4MLn$ have been the most intensively investigated, both experimentally and theo-

* Corresponding authors. E-mail: lapinte@univ-rennes1.fr and halet@univ-rennes1.fr.
[†] Organométalliques et Catalyse.
[‡] Laboratoire de Chimie du Solide et Inorganique Moléculaire.
[§] Groupe Matière Condensée et Matériaux.

(1) Lehn, J.-M. *Supramolecular Chemistry−Concepts and Perspectives*; VCH: Weinheim, 1995.
(2) Ward, M. D. *Chem. Soc. Rev.* **1995**, 121.
(3) McCleverty, J. A.; Ward, D. *Acc. Chem. Res.* **1998**, *31*, 832.
(4) Paul, F.; Lapinte, C. *Coord. Chem. Rev.* **1998**, *178*, 427.
(5) Long, N. J. *Angew. Chem., Int. Ed. Engl.* **1995**, *34*, 21.
(6) Bunz, U. H. F. *Angew. Chem., Int. Ed. Engl.* **1996**, *35*, 969.
(7) Le Narvor, N.; Toupet, L.; Lapinte, C. *J. Am. Chem. Soc.* **1995**, *117*, 7129.
(8) Brady, M.; Weng, W.; Zhou, Y.; Seyler, J. W.; Amoroso, A. J.; Arif, A. M.; Böhme, M.; Frenking, G.; Gladysz, J. A. *J. Am. Chem. Soc.* **1997**, *119*, 775.
(9) Kheradmandan, S.; Heinze, K.; Schmalle, H. W.; Berke, H. *Angew. Chem., Int. Ed.* **1999**, *38*, 2270.
(10) Bruce, M. I.; Low, P. J.; Costuas, K.; Halet, J.-F.; Best, S. P.; Heath, G. A. *J. Am. Chem. Soc.* **2000**, *122*, 1949.
(11) Jiao, H.; Costuas, K.; Gladysz, J. A.; Halet, J.-F.; Guillemot, M.; Toupet, L.; Paul, F.; Lapinte, C. *J. Am. Chem. Soc.* **2003**, *125*, 9511.
(12) Dembinski, R.; Bartik, T.; Bartik, B.; Jaeger, M.; Gladysz, J. A. *J. Am. Chem. Soc.* **2000**, *122*, 810.

10.1021/om050403d CCC: $30.25
Publication on Web 08/11/2005

Scheme 1. Spin Isomers for a Two-Metal-Centered Radical Bridged by an All-Carbon Ligand

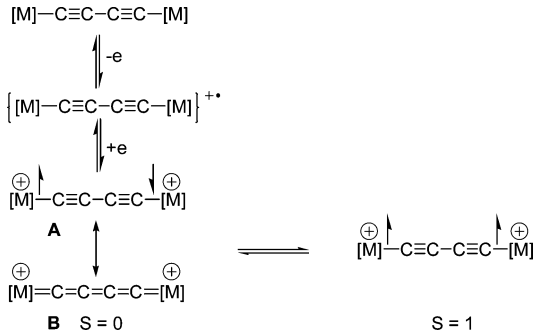

retically. The complexes [Cp*(dppe)Fe−C≡C−C≡C−Fe-(dppe)Cp*] (**1**),[7,13] [Cp*(NO)(PPh_3)Re−C≡C−C≡C−Re-(NO)(PPh_3)Cp*] (**2**),[8] [(I)(dppe)$_2$Mn−C≡C−C≡C−Mn-(dppe)$_2$(I)] (**3**),[9] [Cp(PPh_3)$_2$Ru−C≡C−C≡C−Ru(PPh_3)$_2$-Cp] (**4**),[10] and [Cp*(dppe)Ru−C≡C−C≡C−Ru(dppe)Cp*] (**5**)[14] constitute the most representative examples. All undergo reversible single-electron oxidations and exhibit strong interactions between the metal centers. One-electron chemical oxidations give isolable cation radicals [**1**−**5**]$^+$X$^-$ stable at room temperature. IR and ESR data unambiguously show that the metal termini are equivalent with a formal half positive charge on each metal, and the odd electron is completely delocalized across the wire-like bridge. These mixed-valence compounds are commonly termed "class III" compounds according to the Robin and Day classification.[15]

Further oxidation gives stable dications, and their structure depends on the organometallic building blocks connected to the carbon chain, the oxidation being metal centered (Fe, Mn)[7,9,13] or carbon chain centered (Re, Ru).[8,10,16,17] In-depth investigations have shown that these species exist as a mixture of two spin isomers, the singlet state ($S = 0$) and the triplet state ($S = 1$), which are in equilibrium (Scheme 1). In the singlet state, the valence bond structure of the diradical (**A**) can resonate with the closed-shell structure (**B**), which contributes to the stabilization of the singlet ground state. Magnetic susceptibility measurements clearly established the antiferromagnetic coupling between the two iron spin carriers and allowed the determination of the S/T energy gap (−18.2 cm^{-1}).[16] Experimental data suggest a similar behavior for the Mn derivative **3**,[9,18] whereas the isostructural rhenium and ruthenium complexes (**2**, **4**, **5**) seem to be diamagnetic between 80 and 300 K. The triplet state, too high in energy, cannot be thermally populated.[10,11]

Previous studies on electron conveyors and electron carriers based on redox-active building blocks spanned by polyynediyl structures have clearly shown that the size-expansion of such system is limited by the very poor chemical stability of the species containing unpaired electrons. The size-expansion of the −C_4− carbon chain was successfully accomplished in several cases, but the corresponding oxidized forms are not thermally stable. Indeed, except in the case of the mixed-valence complex [Cp*(dppe)Fe−C≡C−C≡C−C≡C−C≡C−Fe(dppe)Cp*]-[PF_6] (**6**[PF_6], Scheme 2),[19] it was not possible to have access to the corresponding radicals.[12] Introduction of an aromatic ring such as benzene or thiophene in the −C_4− spacer constitutes attractive means to circumvent the instability of the radicals and provides compounds with interesting properties. For example, dications incorporating *para* (**7**[PF_6]$_2$) or *meta* (**8**[PF_6]$_2$) substituted aryl groups revealed an antiferromagnetic or ferromagnetic coupling in the ground state, respectively.[16,20] It also appears that the presence of the thiophene group in the spacer provides a quite stable class III mixed-valence radical (**9**[PF_6]) with an electron delocalization at the molecular level as good as in **6**[PF_6][21] and improves the magnetic coupling between the terminal spin carriers.[22]

Scheme 2. Bis(iron) Complexes Bridged by a Carbon-Rich Ligand

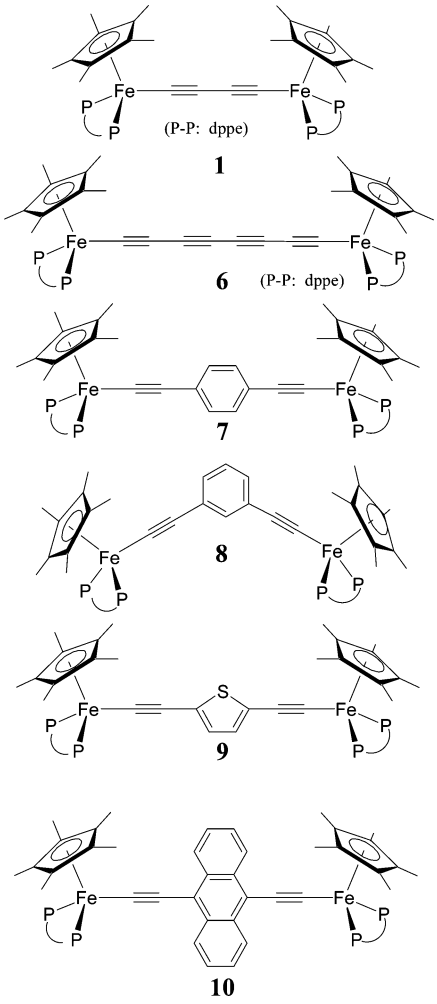

Despite the fact that few reports on binuclear complexes spanned with an anthracene-containing spacer

(13) Guillemot, M.; Toupet, L.; Lapinte, C. *Organometallics* **1998**, *17*, 1928.
(14) Bruce, M. I.; Ellis, B. G.; Low, P. J.; Skelton, B. W.; White, A. H. *Organometallics* **2003**, *22*, 3184.
(15) Robin, M. B.; Day, P. *Adv. Inorg. Chem. Radiochem.* **1967**, *10*, 247.
(16) Le Narvor, N.; Lapinte, C. *C. R. Acad. Sci., Paris, Sér. IIc* **1998**, 745.
(17) Paul, F.; Lapinte, C. In *Unusual Structures and Physical Properties in Organometallic Chemistry*; Gielen, M., Willem, R., Wrackmeyer, B., Eds.; John Wiley & Sons: London, 2002; p 220.
(18) Khan, M. S.; Pasha, N. A.; Kakkar, A. K.; Raithby, P. R.; Lewis, J.; Buhrmann, K.; George, A. V.; Lashi, F.; Malouf, E. V.; Zamello, P. J. *J. Organomet. Chem.* **1992**, *435*, 347.
(19) Coat, F.; Lapinte, C. *Organometallics* **1996**, *15*, 477.
(20) Weyland, T.; Costuas, K.; Mari, A.; Halet, J.-F.; Lapinte, C. *Organometallics* **1998**, *17*, 5569.

have been published, its particular efficiency has been noted in molecular wires built from bis(ruthenium) cyclometalated complexes.[23−25] Recent results also indicate that anthracene favors strong interactions between hydrazine,[26] triarylamine,[27] and porphyrin[28,29] moieties. We then introduced an anthracene fragment in the butadiynediyl bridge spanning two Cp*(dppe)Fe building blocks. The aim was to compare its respective merits with those of the phenyl and thiophene groups in terms of chemical stability of the radicals, electron transfer ability between the remote metal end-groups, magnetic interactions between the spin carriers, and spin distribution between the metal centers and the carbon spacer. In this paper, we report the synthesis of the neutral binuclear complex [Cp*(dppe)Fe−C≡C-9,10-$C_{14}H_8$−C≡C−Fe(dppe)Cp*] (**10**) and its oxidized forms **10**[PF_6], **10**[TCNQ], and **10**[PF_6]$_2$. An extensive analysis of the properties of all the members of this new family of molecules including redox potentials, X-ray determination of the molecular structures, DFT calculations, magnetic property measurements, and Mössbauer, vibrational, and electronic spectroscopies confirms that anthracene efficiently mediates electronic and magnetic interaction between remote spin carriers. It is shown for the first time in the iron series that such an organic group favors carbon-centered oxidation.

Scheme 3[a]

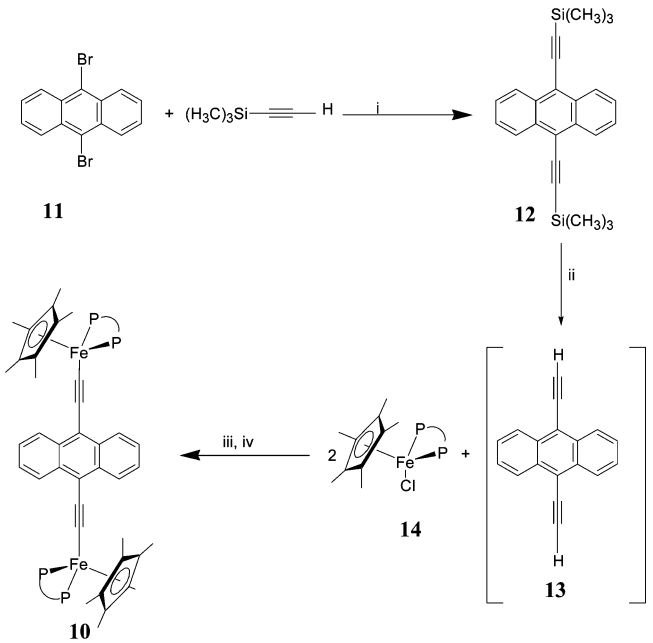

[a] Key reagents: (i) ^{i}Pr$_2$NH, 8% CuI, 4% $PdCl_2(PPh_3)_2$, 70 °C, 16 h; (ii) CH_3OH, 2.2 equiv of K_2CO_3, 20 °C, 10 h; (iii) 2.2 equiv of $NaBPh_4$, 20 °C, 16 h; (iv) 2.2 equiv of KOBu^t, 20 °C, 4 h.

Results and Discussion

1. Synthesis and Characterization of 10. As illustrated in Scheme 3, **10** was synthesized from 9,10-dibromoanthracene, trimethylsilylacetylene, and Cp*(dppe)Fe-Cl (**14**).[30] The 9,10-bis(trimethylsilylethynyl)anthracene (**12**) was prepared by a classical Sonogashira coupling as previously reported. Minor changes in the procedure allowed increasing the yield from 48 to 90%.[31,32] Treatment of **12** with potassium carbonate in methanol provided the 9,10-bis(ethynyl)anthracene, which was in situ reacted with the chloro complex **14** in the presence of sodium tetraphenyl borate. TLC monitoring showed that the organic reagent was consumed after 16 h and the vinylidene intermediate was deprotonated by addition of KOBu^t as previously described for the preparation of **8**.[33] Workup gave **10** as a spectroscopically pure dark blue powder in 91% yield. A FAB mass spectrum of **10** showed the expected parent ion, and the microanalysis was satisfactory. Well-resolved ^{1}H and ^{31}P NMR spectra were obtained, but the weak solubility of **10** in all the usual solvents prevented obtaining the ^{13}C NMR spectrum. Whereas the FTIR spectrum of the free ligand **12** displays two $\nu_{C\equiv C}$ bands at 2147 and 2124 cm^{-1},[25] the spectrum of **10** exhibits a single band at 2010 cm^{-1}. The $\nu_{C\equiv C}$ band is shifted to lower frequency (12 cm^{-1}) relative to that of the mono-iron complex Cp*(dppe)FeC≡C-9-ant (ant = anthracene), which was found at 2022 cm^{-1}.[34] This suggests that the two iron centers significantly interact across the carbon bridge. For purposes of comparison, let us recall that the $\nu_{C\equiv C}$ band was observed around 2050 cm^{-1} in the IR spectrum of the complexes **7**−**9** (Table 1). The presence of the anthracene fragment in the bridge seems to induce a slight increased π-back-bonding donation from the iron center, and it can be anticipated that the metal−metal interaction should be larger in **10** than in the related binuclear derivatives **7**−**9**.

2. Cyclic Voltammetry of 10 and Synthesis of 10$^+$PF$_6^-$, 10$^+$TCNQ$^-$, and 10$^+$2PF$_6^-$. The initial scan in the cyclic voltammogram of **10** from −1.2 to 1.0 V shows two chemically reversible oxidation waves separated by 0.36 V, corresponding to the formation of the radical cation **10**$^+$ and dication **10**$^{2+}$ on the platinum working electrode, respectively (Table 2). A third oxidation, corresponding to the **10**$^{2+}$/**10**$^{3+}$ redox couple, was also observed before the solvent edge.

Interestingly, the first one-electron oxidation appears at a more negative potential in **10** than in the closely related compounds **6**−**9** (Table 2). These data suggest that 9,10-bis(ethynyl)anthracene constitutes both a more efficient and less-electron withdrawing linker than 1,4-bis(ethynyl)benzene or 2,5-bis(ethynyl)thiophene. In other words, the HOMO should have a larger bridging-ligand character in **10** than in compounds **6**−**9**, and as

(21) Le Stang, S.; Paul, F.; Lapinte, C. *Organometallics* **2000**, *19*, 1035.
(22) Roué, S.; Le Stang, S.; Toupet, L.; Lapinte, C. *C. R. Chim.* **2003**, *6*, 353.
(23) Fraysse, S.; Coudret, C.; Launay, J.-P. *J. Am. Chem. Soc.* **2003**, *125*, 5880.
(24) El-gayhouri, A.; Harriman, A.; khatyr, A.; Ziessel, R. *J. Phys. Chem. A* **2000**, *2000*, 1512.
(25) Khan, M. S.; Al-Mandhary, M. R. A.; Al-Suti, M. K.; Al-Battashi, F. R.; Al-Saadi, S.; Ahrens, G.; Bjernemose, J. K.; Mahon, M. F.; Raithby, P. R.; Younus, M.; Chawdhury, N.; Köhler, A.; Marseglia, E. A.; Tedesco, E.; Feeder, N.; Teat, S. J. *Dalton Trans.* **2004**, 2377.
(26) Nelsen, S. F.; Ismagilov, R. F.; Powell, D. R. *J. Am. Chem. Soc.* **1998**, *120*, 1924.
(27) Lambert, C.; Noll, G.; Schelter, J. *Nat. Mater.* **2002**, 69.
(28) Taylor, P. N.; Wylie, A. P.; Huuskonen, J.; Anderson, H. L. *Angew. Chem.* **1998**, *37*, 986.
(29) Piet, J. J.; Taylor, P. N.; Anderson, H. L.; Osuka, A.; Warman, J. M. *J. Am. Chem. Soc.* **2000**, *122*, 1749.
(30) Roger, C.; Hamon, P.; Toupet, L.; Rabaâ, H.; Saillard, J.-Y.; Hamon, J.-R.; Lapinte, C. *Organometallics* **1991**, *10*, 1045.
(31) Scott, L. T.; Necula, A. *Tetrahedron Lett.* **1997**, *11*, 1877.
(32) Kobayashi, E.; Jiang, J.; Furukawa *J. Polym. J.* **1990**, *22*, 266.
(33) Weyland, T.; Lapinte, C.; Frapper, G.; Calhorda, M. J.; Halet, J.-F.; Toupet, L. *Organometallics* **1997**, *16*, 2024.
(34) de Montigny, F.; Argouarch, G.; Lapinte, C. Work in progress.

Table 1. IR $\nu_{C\equiv C}$ Bond Stretching[a] for 10 and Closely Related Complexes

compd	$n = 0$	$n = 1$[b]	$n = 2$[b]	ref
1	2105 (vw)−1959	1973−1880	1950	7
6	2109 (vw)−1949	1879−1784		37
7	2051	2052−1983−1934	1984	46
8	2053	2044−1998	2007	33
9	2054−2039	1977−1910	1941	21
10	2010 (m)	1964 (w)−1901 (vw) 1957−1910[a] 1965−1903[c,d]	1943 (vw)−1896 (w)	this work

[a] Nujol, cm^{-1}. [b] With PF_6 anion unless otherwise specified. [c] With TCNQ anion. [d] KBr.

Table 2. Electrochemical Data for 10 and Closely Related Complexes

compd	$E_{1/2}(0/+1)$,[a] V	$E_{1/2}(+1/+2)$,[a] V	ΔE, V	K_c	$E_{1/2}(+2/+3)$,[a] V	ref
6	−0.27	+0.16	0.43	2.0×10^7	0.98	13
7	−0.27	−0.01	0.26	2.6×10^4	*b*	46
9	−0.39	−0.05	0.34	5.8×10^5	1.04	21
10	−0.40	−0.04	0.36	1.3×10^6	0.94	this work

[a] Cyclic voltammograms recorded in 0.1 M tetra-*n*-butylammonium hexafluorophosphate in CH_2Cl_2, 0.1 V s^{-1}, Pt electrode, V vs SCE (cf. ferrocene/ferricinium 0.460 V vs SCE). [b] Not measured.

Scheme 4[a]

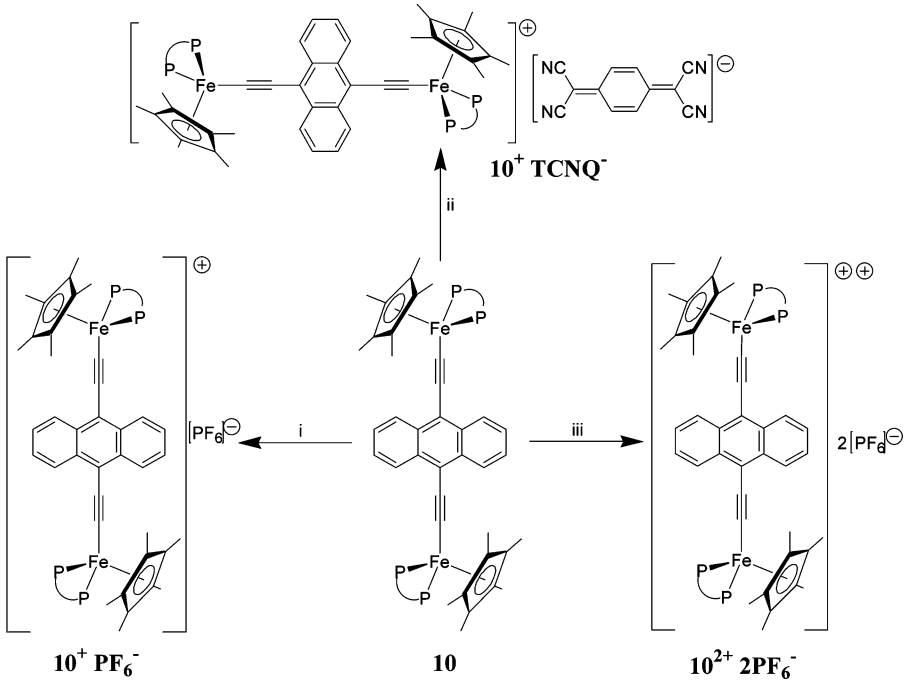

[a] Key reagents: (i) THF, −80 °C, 0.95 equiv of $[(\eta^5\text{-}C_5H_5)_2Fe)]^+PF_6^-$, 16 h; (ii) THF, 1.0 equiv of TCNQ, −80 °C, 16 h; (iii) 1.95 equiv of $[(\eta^5\text{-}C_5H_5)_2Fe)]^+PF_6^-$, −80 °C, 16 h.

a consequence, it can be anticipated that the delocalization of the odd electron is less metal centered in $\mathbf{10}^+$ than in the radicals $\mathbf{6}^+$−$\mathbf{9}^+$ (see DFT results section). In addition, the large wave separation ($\Delta E° = 0.36$ V) between the two first redox processes leads to a large comproportionation constant ($K_c = 1.3 \times 10^6$) and establishes that the MV complex $\mathbf{10}^+$ is thermodynamically very stable in solution.

A current ratio (i_p^a/i_p^c) of unity was determined for the three redox processes, indicating that oxidized forms are stable on the platinum electrode and should constitute accessible synthetic targets. As shown in Scheme 4, $[(\eta^5\text{-}C_5H_5)_2Fe)]\cdot PF_6$ (0.95 equiv) and **10** were reacted in THF at −80 °C. The initial dark blue solution turned dark green after stirring 16 h. Workup gave a black powder of the MV radical $\mathbf{10}\cdot PF_6$ in 67% yield. Similar reaction of **10** and 1.95 equiv of $[(\eta^5\text{-}C_5H_5)_2Fe)]^+ PF_6^-$ gave the dication $\mathbf{10}\cdot 2PF_6$, which was isolated as a green powder in 91% yield. Treatment of **10** with 1.0 equiv of TCNQ in THF at −80 °C provides **10**·TCNQ, isolated as a black powder in 61% yield. A high-resolution mass spectrum (FAB) of $\mathbf{10}\cdot PF_6$, **10**·TCNQ, and $\mathbf{10}\cdot 2PF_6$ showed the expected parent ion $[\mathbf{10}\cdot PF_6]^+$, $[\mathbf{10}\cdot TCNQ]^+$, and $[\mathbf{10}\cdot 2PF_6]^+$. IR data for the three compounds are given in Table 1, and other characterizations are detailed below. As expected, **10** and the corresponding mono- and dicationic salts gave identical cyclic voltammetry. In the particular case of **10**·TCNQ, the redox systems $\mathbf{10}/\mathbf{10}^+$ and $TCNQ^-/TCNQ^{2-}$ were not resolved and gave a two-electron reversible wave at −0.392 V. The redox system $TCNQ^-$/TCNQ was observed at 0.184 V.

3. Molecular Structures of $\mathbf{10}\cdot 2CH_2Cl_2$, 10·TCNQ, and $\mathbf{10}\cdot 2PF_6$. No structural data for any type of

Table 3. Crystallographic Data for $10{\cdot}2CH_2Cl_2$, 10^+TCNQ^-, and $10^{2+}2PF_6^-$

	$10{\cdot}2CH_2Cl_2$	$10^+TCNQ^-{\cdot}2C_5H_{12}$	$10^{2+}2PF_6^-$
molecular formula	$C_{92}H_{90}Cl_4Fe_2P_4$	$C_{224}H_{228}N_8Fe_4P_8$	$C_{50}H_{43}F_6FeP_3$
molecular wt	1573.02	3503.30	906.60
cryst syst	triclinic	monoclinic	monoclinic
space group	$P\bar{1}$	$P2_1/a$	$P2_1/n$
cell dimens			
a, Å	9.587(5)	21.6066 (2)	12.3673 (1)
b, Å	13.173(5)	29.4422 (2)	22.2881 (2)
c, Å	16.586(5)	31.0882 (3)	16.1617 (2)
α, deg	85.882(5)		
β, deg	79.527(5)	91.023 (1)	94.8887 (4)
γ, deg	73.952(5)		
V, Å^3	1979.0(14)	19773.5 (3)	4438.66 (8)
Z	1	4	4
d_{calc}, g/cm^3	1.32	1.177	1.357
T (K)	293 (2)	293 (2)	293 (2)
abs coeff, mm^{-1}	0.629	0.407	0.507
F(000)	822	7408	1872
cryst dimens, mm	0.12 × 0.05 × 0.03	0.35 × 0.24 × 0.24	0.35 × 0.12 × 0.12
diffractometer	Enraf Nonius FR590	Nonius Kappa CCD	Nonius Kappa CCD
radiation, Å	Mo Kα (0.71069)	Mo Kα (0.71073)	Mo Kα (0.71069)
data collection method	$\omega/2\theta$	$\omega/2\theta$	$\omega/2\theta$
t_{max}/measure, s	60	60	60
range/indices (h,k,l)	−12, 11; −17, 17; −21, 20	0, 28; 0, 38; −40, 40	0, 16; 0, 28; −20, 20
θ range	2.037 to 27.485	1.53 to 27.52	1.56 to 27.48
no. of reflns measd	9076	44451	10146
no. of obsd data, $I>2\sigma(I)$	5023	23515	8075
no of variables	460	2053	529
R_{int} (from merging equiv reflns)			
final R	0.0653	0.0938	0.0525
	[R_w = 0.1509]	[R_w = 0.2595]	[R_w = 0.1383]
R indices (all data)	0.132	0.1790	0.0700
	[R_w = 0.1842]	[R_w = 0.3202]	[R_w = 0.1525]
GOF	1.021	1.043	1.087
largest diff peak and hole, e Å^{-3}	0.60, −0.80	2.33, −0.68	1.61, −0.61

bimetallic complex containing a 9,10-diethynylanthracene bridge have been reported to date. To help in understanding the structural reorganization of the bis(ethynyl)anthracene bridge occurring upon oxidation, the crystal structures of $\mathbf{10{\cdot}2}CH_2Cl_2$, $\mathbf{10{\cdot}}$TCNQ and $\mathbf{10{\cdot}}2PF_6$ were determined by single-crystal X-ray crystallography, as reported in Table 3 and the Experimental Section. The molecular structures are shown in Figure 1, and salient distances and angles are given in Table 4.

Crystals of $\mathbf{10{\cdot}}2CH_2Cl_2$ were grown by slow diffusion of pentane in a CH_2Cl_2 solution of the neutral complex. Single crystals of the salts $\mathbf{10{\cdot}}$TCNQ and $\mathbf{10{\cdot}}2PF_6$ were obtained by diffusion of pentane in a THF solution of the corresponding compound. It is noteworthy that all attempts to grow crystals from $\mathbf{10{\cdot}}PF_6$ using either the CH_2Cl_2/pentane or THF/pentane combinations of solvents provided crystals of $\mathbf{10{\cdot}}2PF_6$ as the unique crystallized material. This illustrates that despite a very large comproportionation constant, which makes the concentration ratio [$\mathbf{10{\cdot}}PF_6$]/[$\mathbf{10{\cdot}}2PF_6$] > 1000, only the less soluble derivatives gave X-ray suitable crystals. Complexes $\mathbf{10{\cdot}}2CH_2Cl_2$ and $\mathbf{10{\cdot}}2PF_6$ crystallize in the triclinic space group $P\bar{1}$ and monoclinic space group $P2_1/n$, respectively, and both have a center of inversion, which makes the two organoiron units strictly equivalent and the planes of the two Cp* rings parallel. The MV salt $\mathbf{10{\cdot}}$TCNQ crystallizes in the monoclinic space group $P2_1/a$, and two nonequivalent molecules were found in the unit cell. As a consequence, the structural parameters are less accurate in the case of the mixed-valence complex.

As expected from many earlier structures of related mononuclear and binuclear cyclopentadienyl complexes, the iron end-groups exhibit formally octahedral geometries, with bond lengths and angles in previously established ranges.[4,7,35,36] However, considering the series $\mathbf{10{\cdot}}n PF_6$ (n = 0−2), several changes in individual bond lengths can be discerned as oxidation proceeds. Thus, as n increases, the Fe−P distances increase. These changes are consistent with some reduction in the π-back-bonding from the metal centers to the phosphine ligands. It is interesting to note that the elongation of the Fe−P bond lengths in $\mathbf{10}^+$ vs **10** (ca. 0.8%) is somewhat smaller than the that in $\mathbf{10}^{2+}$ vs $\mathbf{10}^+$ (ca. 1.6%). Oxidation also results in pronounced changes in the metrical parameters associated with the M−C_2−ant−C_2−M chain. The Fe−C bond distances decrease 3% from **10** to $\mathbf{10}^+$ and 1% from $\mathbf{10}^+$ to $\mathbf{10}^{2+}$. Similarly, the first oxidation induces both more pronounced lengthening of the C≡C triple bond and shortening of the C−C single bond between the ethynyl and anthracenyl fragments than the second oxidation. Comparison of the CC bond distances in the anthracene fragment reveals that this part of the molecule remains unchanged as the oxidation proceeds, or at least the changes are too small to be detected by the X-ray analysis. Taken as a whole, the X-ray parameters indicate that oxidation leads to structural changes both in the metal coordination sphere and in the alkynyl ligands. However, if the

(35) Denis, R.; Toupet, L.; Paul, F.; Lapinte, C. *Organometallics* **2000**, *19*, 4240.
(36) Argouarch, G.; Thominot, P.; Paul, F.; Toupet, L.; Lapinte, C. *C. R. Chim.* **2003**, *6*, 209.

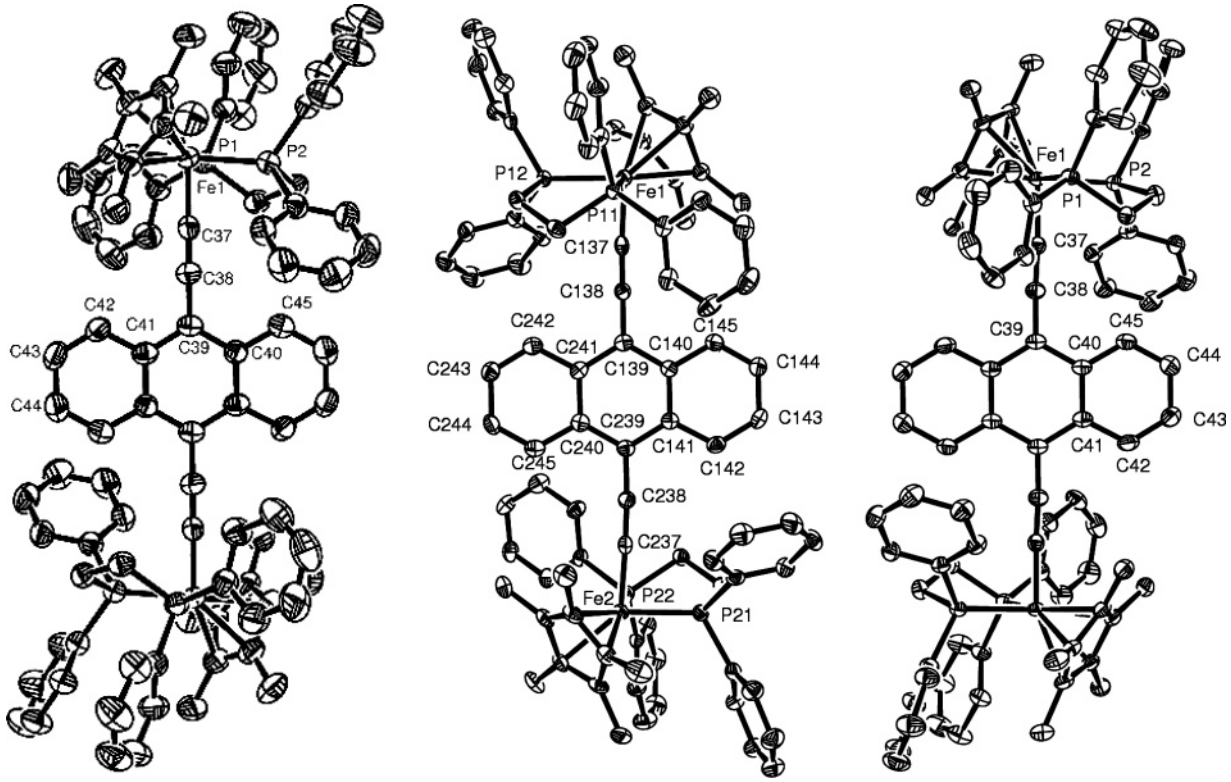

Figure 1. Drawings of **10** (left), **10**·TCNQ (center), and **10**·2PF_6 with atomic numbering. Thermal ellipsoids are at the 50% probability level. Hydrogen atoms, solvent molecules, and counteranions are omitted for clarity.

second oxidation seems to be metal centered, as usually observed in the Cp*(dppe)Fe series, the first oxidation should present a dominant carbon character. Such a behavior, common in Ru or Re alkynyl series, is unprecedented in the iron series.

4. DFT Results. A theoretical study was then conducted in order to shed light on the original behavior of the title compound due to the anthracene fragment. Density functional (DF) molecular orbital (MO) calculations were first carried out on the hydrogen-substituted model complex (η^5-C_5H_5)(η^2-dpe)Fe−C≡C-9,10-ant-C≡C−Fe(η^2-dpe)(η^5-C_5H_5) (**10-H**, dpe = H_2P−$(CH_2)_2$−PH_2) to further the understanding of the geometry and the electronic structure of compound **10**. For comparative purposes, previous results obtained on the related neutral compounds (η^5-C_5H_5)(η^2-dpe)Fe−C≡C−C≡C−Fe(η^2-dpe)(η^5-C_5H_5), **1-H**, (η^5-C_5H_5)(η^2-dpe)Fe−C≡C−C≡C−C≡C−C≡C−C≡C−Fe(η^2-dpe)(η^5-C_5H_5), **6-H**,[37] (η^5-C_5H_5)-(η^2-dpe)Fe−C≡C-1,4-C_6H_4−C≡C−Fe(η^2-dpe)(η^5-C_5H_5), **7-H**,[20] and their oxidized forms are recalled. In the interest of internal consistency in the data, new calculations were performed on **7-H**.

Optimized Geometries. Pertinent optimized structural parameters for the different studied models are reported in Table 5. The optimized geometry of **10-H** compares rather well with the X-ray structure of **10** (see Tables 4 and 6). As often noted when Cp and dpe are used for Cp* and dppe, respectively, the calculated Fe−C(Cp) and Fe−P(dpe) distances are somewhat too short with respect to those measured in the experimental compounds.[38] For the rest of the neutral molecule, the largest bond distance deviation between the experimental and optimized structures concerns the Fe−C137 bond (0.03 Å). Such a deviation between theory and experiment is typical for this kind of organometallic compound containing conjugated carbon spacers.[11,20] A structural comparison of **10-H** with **7-H** indicates that the C−C bond lengths in the inner ring of the anthracene moiety in the former are significantly longer than the corresponding C(240)−C(241) lengths in the benzene ring in the latter (0.05 Å on average, see Table 5 and Figure 2).

Of particular interest is the geometry of [**10-H**]$^{2+}$, which can theoretically exhibit different spin configurations. [**10-H**]$^{2+}$ was optimized in its two possible spin states, i.e., singlet and triplet. The singlet state is largely energetically favored over the triplet state (ΔE_{ST} = 0.425 eV (ca. 3420 cm^{-1})). Additional calculations using the broken-symmetry formalism were performed in order to better estimate the singlet−triplet energy gap (ΔE_{ST}). They did not show any asymmetry for the optimized geometry of [**10-H**]$^{2+}$. Similar calculations carried out on [**7-H**]$^{2+}$ lead to a broken symmetry singlet, computed to be isoenergetic to the triplet state. Interestingly, with a C_4 conjugated chain, the triplet and singlet states of [**1-H**]$^{2+}$ are also isoenergetic within the limits of accuracy of the method used. But in contrast to [**7-H**]$^{2+}$, the geometry of the singlet is symmetric. These different results reflect the dramatic changes that may be induced upon the modification of the carbon spacer in this kind of molecule. Obviously, a bis(ethynyl)anthracene bridge favors the singlet spin state of the dication **10**$^{2+}$.

The computed geometry of the singlet [**10-H**]$^{2+}$ is in relative good agreement with the X-ray data of **10**$^{2+}$ with deviations up to 0.06 Å for Fe−C37 and 0.03 Å for C37−C38. Nevertheless, the geometrical changes com-

(37) Coat, F.; Paul, F.; Lapinte, C.; Toupet, L.; Costuas, K.; Halet, J.-F. *J. Organomet. Chem.* **2003**, *683*, 368.
(38) Costuas, K.; Saillard, J.-Y. *Organometallics* **1999**, *18*, 2505.

Table 4. Selected Distances (Å) and Angles (deg) for $10\cdot 2CH_2Cl_2$, 10^+TCNQ^-, and $10^{2+}2PF_6^-$

	$10\cdot 2CH_2Cl_2$	$10^{2+}2PF_6^-$		10^+TCNQ^-[a]
Fe1−P1	2.1787(14)	2.2304 (7)	Fe1−P11	2.1990(15), 2.2068(16)
Fe1−P2	2.1845 (14)	2.2400 (7)	Fe1−P12	2.1932(15), 2.201 0(14)
			Fe2−P21	2.1924(16), 2.2008(15)
			Fe2−P22	2.2048(15), 2.2086(16)
Fe−C37	1.895 (4)	1.819 (3)	Fe1−C137	1.840 (5), 1.845 (5)
			Fe2−C237	1.845 (5), 1,835 (6)
C37−C38	1.226 (5)	1.237 (4)	C137−C138	1.248 (7), 1.236 (7)
			C237−238	1.232 (7), 1.237 (8)
C38−C39	1.421 (5)	1.394 (3)	C138−C139	1.392(7), 1.408(7)
			C238−C239	1.406(7), 1.416(7)
C39−C40	1.424(5)	1.447(4)	C139−C140	1.430(7), 1.431(7)
			C239−C240	1.425(8), 1.432(7)
C40−C41	1.425(7)	1.421(7)	C140−C141	1.418(7), 1.420(7)
			C240−C241	1.421(7), 1.421(7)
C41−C42	1.418(6)	1.409(4)	C141−C142	1;418(8), 1.416(8)
			C241−C242	1.429(8), 1.411(8)
C42−C43	1.358(6)	1.370(4°	C142−C143	1.371(8), 1.352(8)
			C242−C243	1.345(8), 1.379(8)
C43−C44	1.402(6)	1.408(4)	C143−C144	1.409(8), 1.420(8)
			C243−C244	1.427(8), 1.407(8)
C44−C45	1.363(6)	1;366(4)	C144−C145	1.364(8), 1.358(8)
			C244−C245	1.346(8), 1.365(8)
C45−C40	1.413(5)	1.412(4)	C145−C140	1.437(7), 1.419(7)
			C245−C140	1.425(7), 1.418(7)
Fe1−Cp[b]	1.745	1.771	Fe1−Cp1[b]	1.758, 1.762
			Fe2−Cp2[b]	1;760, 1.754
Fe1−Fe1	11.97	11.77	Fe1−Fe2	11.8, 11.8
P1−Fe1−P2	85.42(5)	84.76(3)	P11−Fe1−P12	85.16(6), 85.07(6)
			P21−Fe2−P22	84.98(6), 84.97(6)
P1−Fe1−C37	84.67(12)	87.79(8)	P11−Fe1−C137	84.98(16), 84.77(17)
			P21−Fe2−C237	86.91(16), 84.36(18)
Fe1−C37−C38	178.8(4)	176.82(3)	Fe1−C137−C138	176.6(5), 177.2(5)
			Fe2−C237−C238	177.9(5), 176.0(5)
C37−C38−C39	178.7(4)	173.6(3)	C137−C138−C139	174.8(5), 175.5(6)
			C237−C238−C239	175.3(6), 172.8(6)
C38−C39−C40	121.0(3)	119.6(2)	C138−C139−C140	120.8(5), 120.9(5)
			C238−C239−C240	120.4(5), 120.1(5)
Cp[b]−Fe1−Fe1−Cp[b]	180	180	Cp[b]1−Fe1−Fe2−Cp[b]1	180, 180

[a] Values for molecules 1 and 2 are given. [b] Centroid of the η^5-C_5Me_5 ligand.

puted upon oxidation confirm the trends measured experimentally. The metal−ligand distances (Cp, dpe) are significantly elongated, whereas the Fe−C(37) bond is shortened. To a lesser extent, the C(37)−C(38) triple bond and the C(38)−C(39) single bond are both theoretically and experimentally lengthened and shortened, respectively. Geometrical changes upon oxidation within the anthracene ring, i.e., a shortening and a lengthening of one C−C bond over two, are quite weak (max. 0.03 Å). The calculated C−C distances of the central ring of the anthracene suggest some quinonic character in the dication. The C−C bond in the ethynyl moieties lengthens substantially upon oxidation, as usually observed for this kind of species.[11,20] The mono-oxidized compound $[\mathbf{10\text{-}H}]^+$ shows a geometrical arrangement intermediate between those of **10-H** and $[\mathbf{10\text{-}H}]^{2+}$. A careful analysis of the coordination sphere arrangement of the metal reveals that, as experimentally observed, the geometrical changes upon oxidation are less important between the monocation and the dication than between the neutral compound and the monocation. For instance, the Fe−C(Cp) and Fe−P distances are proportionally 2 times less elongated after the second oxidation process than after the first one.

In contrast to **10-H**, the Fe−C(Cp) and Fe−P distances are equally affected in **7-H** upon the first and the second oxidations. The lengthening of the conjugated spacer from C_4 to C_8, $C_2-C_6H_4-C_2$, or C_2-ant-C_2 leads to some contraction of the Fe−C bond distances, from 1.917 to 1.867, 1.879, and 1.864 Å, respectively (see Table 5). This confirms the experimental observations. It is noteworthy that there is no noticeable difference in the metal−alkyne distances between the related compounds **6-H**, **7-H**, and **10-H**, which contain linkers of comparable length.

Electronic Structures. The density functional molecular orbital (DF-MO) diagram of **10-H** is shown on the right-hand side of Figure 3. For comparative purposes, the DF-MO diagrams of **1-H**, **6-H**, and **7-H** are recalled on the left-hand side of Figure 3. The HOMO/LUMO gap of **10-H** is large (1.41 eV) but significantly smaller than that found for the other computed complexes, in particular with the benzene-containing compound **7-H** (1.87 eV for **7-H**, 1.64 eV for **6-H**, and 1.46 eV for **1-H**). It is noteworthy that the HOMO of **10-H** is rather high in energy and is separated by a significant energy gap (0.77 eV) from the rest of the occupied orbitals. This HOMO is π-type in character, antibonding between Fe and C(37) and bonding between C(37) and C(38). This is a common feature for carbon spacer-containing organometallic species.[10,33] This MO features an important contribution on anthracene (38%) and to a lesser extent on Fe (23%) and the ethynyl groups (29%). Replacement of the central anthracene moiety by a benzene ring in **7-H** modifies this distribution since the percentage on the central entity drops to 17%

Table 5. Pertinent Optimized Bond Lengths (Å) for Models [1-H]$^{n+}$, [6-H]$^{n+}$, [7-H]$^{n+}$, and [10-H]$^{n+}$ (n = 0−4) Compared with Corresponding Experimental Data (in italics when available)

	1-H	[**1-H**]$^{+}$	[**1-H**]$^{2+}$ (S=0)	[**1-H**]$^{2+}$ (S=1)	**6-H**	[**6-H**]$^{+}$	**7-H**	[**7-H**]$^{+}$	[**7-H**]$^{2+}$ (S=0)	[**7-H**]$^{2+}$ (BS)[a]	[**7-H**]$^{2+}$ (S=1)	**10-H**	[**10-H**]$^{+}$	[**10-H**]$^{2+}$ (S=0)	[**10-H**]$^{2+}$ (S=1)
Fe1−C137	1.913	1.851	1.796	1.794	1.847	1.778	1.867	1.801	1.749	1.760	1.788	1.874	1.806	1.756	1.803
	1.884(3)[11]	*1.830(8)*			*1.864(4)*[37]							*1.895(4)*	*1.841(5), 1.845(5)*	*1.819 (3)*	
C137−C138	1.246	1.259	1.276	1.279	1.254	1.268	1.240	1.249	1.262	1.264	1.252	1.240	1.252	1.264	1.253
	1.220(4)	*1.236(9)*			*1.222(4)*							*1.227(5)*	*1.247(5), 1.232(5)*	*1.237 (4)*	
C138−C139	1.365	1.339	1.314	1.313	1.346	1.323	1.423	1.400	1.378	1.382	1.406	1.416	1.394	1.372	1.404
	1.373(4)	*1.36(1)*			*1.369(4)*							*1.419*		1.394 (3)	
Fe1−P[b]	2.164	2.190	2.225	2.233	2.123	2.150	2.116	2.141	2.168	2.135	2.187	2.121	2.148	2.162	2.171
	2.169(1)				*2.194(1)*										
Fe1−Cp[c]	1.752	1.771	1.783	1.793	1.692	1.716	1.694	1.706	1.732	1.740	1.737	1.697	1.716	1.725	1.732
	1.737	*1.766*			*1.743*							*1.745*	*1.758, 1.752*	*1.771*	
Fe2−C237	1.913	1.852	1.796	1.794	1.868	1.804	1.891	1.825	1.775	1.784	1.816	1.855	1.806	1.756	1.832
	1.889(3)				*1.862(4)*								*1.845(5), 1.835(5)*		
C237−C238	1.246	1.259	1.276	1.279	1.251	1.265	1.240	1.249	1.262	1.263	1.252	1.242	1.252	1.264	1.251
	1.220(4)				*1.228(4)*								*1.237(5), 1.237(5)*		
C238−C239					1.345	1.321	1.424	1.400	1.379	1.383	1.407	1.416	1.394	1.372	1.405
Fe2−P[b]	2.164	2.190	2.225	2.233	2.123	2.149	2.123	2.144	2.170	2.119	2.183	2.117	2.148	2.162	2.175
	2.169(1)	*2.206(2)*			*2.191(1)*										
Fe2−Cp[c]	1.750	1.771	1.793	1.794	1.697	1.720	1.687	1.718	1.725	1.728	1.736	1.691	1.716	1.725	1.727
	1.737				*1.746*								*1.760, 1.754*		

[a] Broken-symmetry singlet state. [b] Average. [c] Centroid of the η^5-C_5H_5 ligand.

Table 6. Atomic Spin Densities Calculated for [1-H]$^{+}$, [7-H]$^{+}$, [7-H]$^{+}$, and [10-H]$^{+}$

	[**1-H**]$^{+}$	[**6-H**]$^{+}$	[**7-H**]$^{+}$	[**10-H**]$^{+}$
Fe1	0.32	0.22	0.27	0.19
C37	0.11	0.09	0.07	0.10
C38	0.08	0.06	0.10	0.05
C39		0.07	0.04	0.10
C40		0.06	0.02	0.01
C41			0.02	0.01
C42				0.02
C43				0.02
C44				0.01
C45				0.02
Fe2	0.32	0.22	0.27	0.19
C37′	0.11	0.09	0.07	0.10
C38	0.08	0.06	0.09	0.05
C39′		0.09	0.02	0.10
C40′			0.02	0.01
C41′				0.01
C42′				0.02
C43′				0.02
C44′				0.01
C45′				0.02

(Figure 3). Interestingly, the LUMO of **10-H** is rather low in energy with respect to the LUMO of the other congeners and is mainly anthracene in character (77%). This contrasts with the LUMO of the related systems such as **6-H** and **7-H**, which is metal−ligand (Cp, dpe) based. The presence of an anthracene-based low-lying unoccupied orbital in the MO diagram is partly responsible for the relatively small HOMO/LUMO energy gap with respect to that in **6-H** and **7-H**. This may influence the MLCT and consequently the optical properties of **10**.

Ionization Potentials. Carbon-rich organoiron compounds are well known to undergo several successive oxidations.[4] As shown earlier, **10** can also be oxidized, even more easily than the closely related complexes **6** and **7** (see Table 2). The adiabatic ionization potentials (IPs) were computed for different complexes and compared. With a first ionization potential of 4.83 eV, **10-H** is more readily ionized than its congeners **6-H** and **7-H**, the first IPs of which are 4.94 and 4.99 eV, respectively. This value is close to 4.79 eV, the first IP for model **1-H**, reflecting that **10-H** and **1-H** have comparable electron-releasing properties. Even though the solution-phase oxidation potentials and the calculated ionization potentials are not directly comparable (solvation effect), they track rather well the computed gas-phase IPs. Indeed, the cyclic voltammetry data show the same trend, i.e., the ease of $E_1(0/1+)$ oxidation being **1** (−0.69 V) > **10** (−0.40 V) > **6** (−0.27 V) ∼ **7** (−0.27 V) (see above). Although Koopmans' theorem does not apply, it is interesting to note that this trend is also in agreement with the energy order of the HOMOs (−3.12 eV for **1-H**, −3.39 eV for **10-H**, −3.47 eV for **6-H**, and −3.49 eV for **7-H**). As said earlier, the HOMO in **10-H** is higher in energy with respect to that of **6-H** and **7-H**.

Computed second IPs indicate that that of **10-H** (7.80 eV) is smaller than that of **7-H** (8.04 eV). Cyclic voltammetry data show the same trend since **10**$^{+}$ is 0.20 and 0.03 V thermodynamically easier to oxidize than complexes **6**$^{+}$ and **7**$^{+}$, respectively.

Spin Densities. Atomic spin densities were computed and compared for different monocations in order to probe the delocalization of the unpaired electron. As

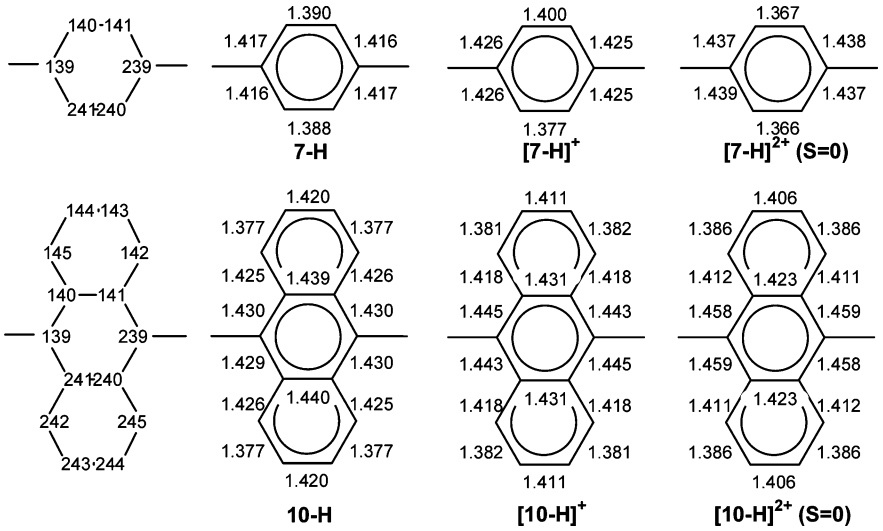

Figure 2. Atom numbering (left) and DFT-optimized intercycle carbon−carbon distances (Å) in [**7-H**]$^{n+}$ and [**10-H**]$^{n+}$ (n = 0−2) (right).

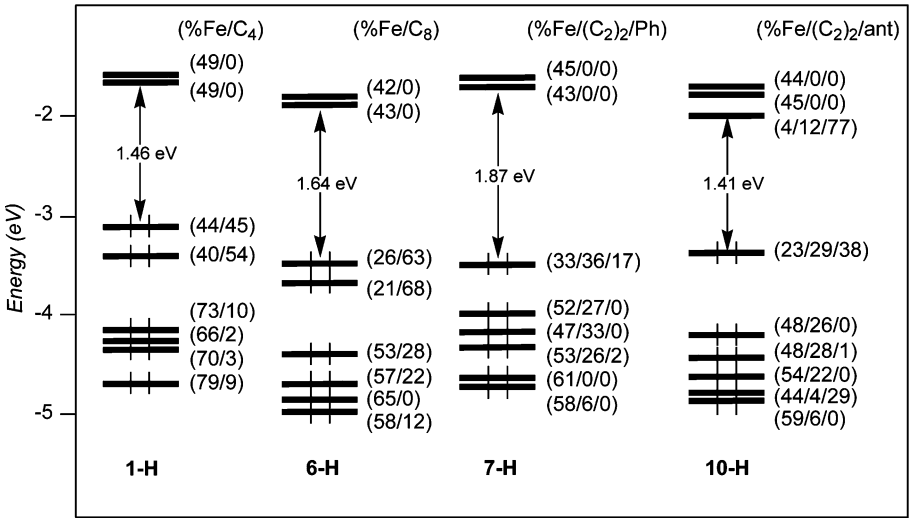

Figure 3. DFT MO diagrams of **1-H**, **6-H**, **7-H**, and **10-H**. The metal/carbon chain percentage contributions of the MOs are given in brackets.

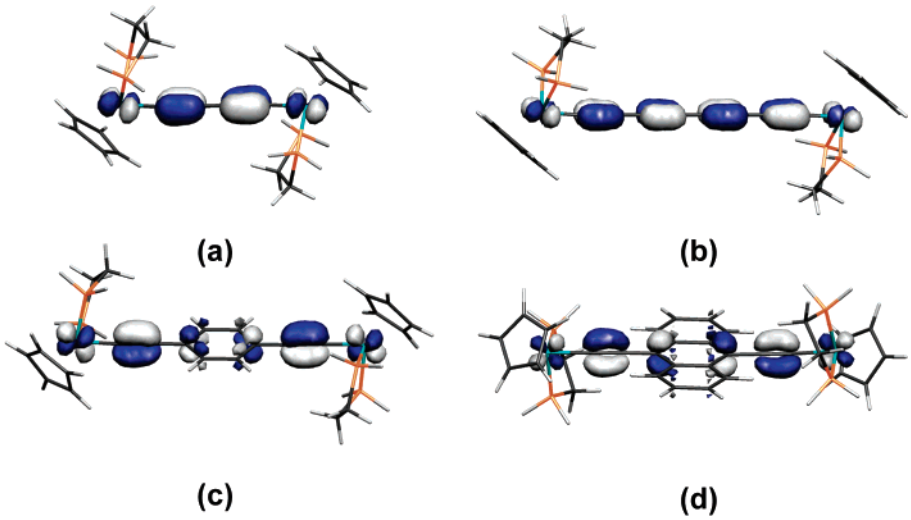

Figure 4. DFT contour plots of the HOMO for the model complexes **1-H** (a), **6-H** (b), **7-H** (c), and **10-H** (d). Contour values are ±0.05 (e/bohr^3)$^{1/2}$.

shown in Table 6, the spin density distribution computed for [**10-H**]$^+$ differs substantially from that computed for the systems with other carbon bridges such as C_4, C_8, or bis(ethynyl)benzene. The total metallic spin density is much smaller in [**10-H**]$^+$ than in the other compounds (0.38 vs 0.64, 0.44, and 0.54 for [**1-H**]$^+$,

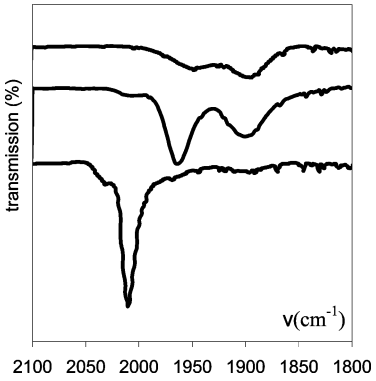

Figure 5. IR spectra (Nujol mull) of **10** (bottom), **10**·PF_6 (middle), and **10**·$2PF_6$ (top).

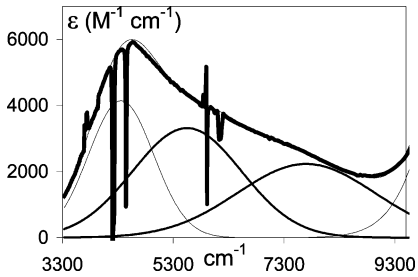

Figure 6. NIR absorption spectral data for **10**·PF_6 (bold line) in CH_2Cl_2 and the deconvoluted ICT bands.

[**6-H**]$^+$, and [**7-H**]$^+$, respectively). It turns out that the major part of the spin density is localized in a noneven manner on the carbon spacer. The contribution is mainly found on the ethynyl units and on the *ipso* carbon of the anthracene ring.

5. ^{1}H NMR Spectroscopy and Magnetic Properties of 10·*n*PF_6. The ^{1}H, ^{31}P, and ^{13}C NMR spectra recorded for the two complexes **10**·*n*PF_6 (n = 0, 2) in solution are well-resolved and quite similar. In the proton NMR spectra, the resonance of the C_5Me_5 ligand, which is very sensitive to the presence of an unpaired electron on the iron center,[7,30] is observed at almost the same position in the dication (δ 1.46) and the neutral complex (δ 1.65). This observation indicates that the electronic structure of **10**·$2PF_6$ should be very different of those of **1**·$2PF_6$ and (**6**−**9**)·$2PF_6$, for which a dominant triplet state contribution was found at 293 K.[7] The ^{31}P resonance of the dppe ligand, which is also very sensitive to the presence of spin density on the iron center, greatly supports the ^{1}H conclusion. Indeed, the ^{31}P NMR spectrum displays a well-resolved sharp singlet for the phosphorus atom resonance at δ 69.1 ppm, in contrast with the behavior of the paramagnetic organometallic complexes, for which the ^{31}P resonances are generally not observed.[20,39] This is particularly true for the 17-electron species of the [Cp*(dppe)Fe(III)R]$^+$ series.[20] In addition, in the case of binuclear complexes a strong line broadening is a diagnostic of singlet−triplet exchange.[40] Surprisingly enough, one notes the strong downfield shielding, which suggests that the magnetic environment of the phosphorus nuclei is magnetically unusual. The ^{13}C NMR spectrum of **10**·$2PF_6$ displays resonances at δ 271.2 and 144.4 attributed to the α and β carbon atoms, respectively, in accord with a cumulene-like structure for **10**·$2PF_6$.

The diamagnetic character of this complex was also probed by the determination of the magnetic moment in solution (CD_3COCD_3) by the Evans method.[41,42] A very weak negative value was found for μB as invariably found for diamagnetic compounds. In addition, the chemical shift is independent of the temperature in the range 190−300 K, confirming once again that the contribution of the triplet state of this molecule is not detectable in this range of temperature.[43,44] Considering the accuracy of the measurement, it can be assumed that the triplet state is less than 1% at 293 K and the singlet-to-triplet energy gap should be smaller than −1200 cm^{-1}. The corrected molar magnetic susceptibility of a powdered sample of **10**·$2PF_6$ was determined by SQUID measurement in the range 4−300 K. A plot of the product $\chi_M T$ vs T is linear. The intercept is very close to zero, indicating the diamagnetic nature of the sample.[45] The temperature dependence of χ_M is inconsistent with a thermally populated triplet excited state.

6. IR Spectroscopy. A comparison of the IR spectra of the three complexes **10**·*n*PF_6 (n = 0, 1, 2) in Figure 5 clearly shows that the relative intensities of the bands decrease as oxidation proceeds. In addition, the IR spectra of oxidized forms (n = 1, 2) display two bands located at lower energy than the unique band observed in the spectrum of their neutral precursor **10** (Table 1). This indicates a reduced bond order for the carbon bonds of the bridging ligand in the oxidized species, consistent with an increased contribution of "cumulenoid" or other resonance structures with reduced triple-bond character. Two ν_{CC} band stretches were also observed for the radical cations **7**$^+$, **8**$^+$, and **9**$^+$, but at higher frequencies than those found for **10**$^+$.[21,46,47] Only absorption bands at lower frequencies were found for the MV complexes **1**$^+$ and **6**$^+$, where the two iron centers are spanned by an all-carbon chain.[7,19] The band stretches found in the IR spectrum of the dication **10**$^{2+}$ are located at frequencies lower than those previously observed for any other dications of this series (Table 1). These results seem to indicate that the change in carbon bonding is larger after the first oxidation than after the second oxidation. This is in agreement with the DFT results (see above).

7. Mössbauer Spectroscopy. The use of ^{57}Fe Mössbauer spectroscopy for the study of MV species is particularly interesting.[48−54] It allows a precise knowl-

(39) Fettinger, J. C.; Mattamana, S. P.; Poli, R.; Rogers, R. D. *Organometallics* **1996**, *15*, 4211.
(40) Guillaume, V.; Mahias, V.; Mari, V.; Lapinte, C. *Organometallics* **2000**, *19*, 1422.
(41) Evans, D. F. *J. Chem. Soc.* **1959**, 2003.
(42) Sur, S. K. *J. Magn. Reson.* **1989**, *82*, 169.
(43) La Mar, G. N.; Eaton, G. R.; Holm, R. H.; Walker, F. A. *J. Am. Chem. Soc.* **1973**, *95*, 63.
(44) Bertini, I.; Luchinat, C. *NMR of Paramagnetic Molecules in Biological Systems*; The Benjamin/Cummings Publishing Company, Inc.: Menlo Park, CA, 1986.
(45) Kahn, O. *Molecular Magnetism*; VCH Publishers: New York, 1993.
(46) Le Narvor, N.; Lapinte, C. *Organometallics* **1995**, *14*, 634.
(47) Weyland, T.; Costuas, K.; Toupet, L.; Halet, J.-F.; Lapinte, C. *Organometallics* **2000**, *19*, 4228.
(48) Greenwood, N. N. *Mössbauer Spectroscopy*; Chapman and Hall: London, 1971.
(49) Dong, T.-Y.; Hendrickson, D.; Pierpont, C. G.; Moore, M. F. *J. Am. Chem. Soc.* **1986**, *108*, 963.
(50) Moore, M. F.; Wilson, S. R.; Cohn, M. J.; Dong, T. Y.; Kampara, T.; Hendrickson, D. N. *Inorg.* Chem. **1985**, *24*, 4559.
(51) Dong, T.-Y.; Kampara, T.; Hendrickson, D. N. *J. Am. Chem. Soc.* **1986**, *108*, 5857.
(52) Kampara, T.; Hendrickson, D. N.; Dong, T.-Y.; Cohn, M. J. *J. Chem. Phys.* **1987**, *86*, 2362.

Table 7. ^{57}Fe Mössbauer Parameters for $10^{n+}x\mathrm{X}^-$ and Closely Related Iron Complexes

	IS[a] (QS), mm s^{-1}			
compd	$n = 0$	$n = 1$	$n = 2$	ref
1	0.27 (2.07)	0.21 (1.32)	0.18 (1.05)	7
6	0.24 (1.94)	0.24 (1.91) 0.21 (1.45) 0.88 (0.11)	unknown	13
7	0.265 (2.020)	0.248 (1.961) 0.203 (1.111) 0.246 (0.710)	0.239 (0.911)	46
8	0.20 (2.00)	0.25 (2.00) 0.25 (0.85)	0.28 (0.89)	33
9	0.255 (1.984)	0.212 (1.444)	0.181 (1.024)	21
10	0.262 (1.958)	0.188 (1.206)[c]	0.171 (1.146)	this work

[a] The velocity is referenced to iron metal. [b] With PF_6 anion unless otherwise specified. [c] With TCNQ anion.

edge of iron centers, including the determination of the oxidation states, the estimation of the spin distribution between the remote end-groups and the organic bridge, and the evaluation of the electron transfer rate relative to the acquisition time of the technique.[55] Indeed, for a bis-iron MV compound, the presence of two distinct doublets in the spectrum indicates a localized valence with a rate constant $k_e > 10^{-6}$ s^{-1}, whereas observation of a single averaged doublet is a diagnostic of a detrapped valence with $k_e < 10^{-9}$ s^{-1}.[56] In addition, it has recently been shown that ^{57}Fe Mössbauer spectroscopy can provide a better understanding of the Fe=C bonding in mononuclear metallacumulenylidenes of the Cp*(dppe)Fe series. In particular, it can shed some light on the strength of the iron π-back-bonding to cumulenylidene ligands.[36]

The Mössbauer spectra of the three compounds **10**, **10**·TCNQ, and **10**·2PF_6 were run at 80 K and least-squares fitted with Lorentzian line shapes.[57] The isomer shift (IS) and quadrupole splitting (QS) parameters are given in Table 7. The spectrum of the neutral complex **10** exhibits a single doublet with IS and QS parameters typical of Fe(II) complexes in the Cp*(dppe)Fe series. In the case of the dicationic complex **10**·2PF_6, the IS parameter is close to the values previously reported for the binuclear dications **1** and **6**−**9**. Nevertheless it appears to be the smallest value found in these series of compounds. In addition, one notes that the IS is quite close to the data found for mononuclear cationic cumulenylidene iron complexes [Cp*(dppe)Fe=(C)$_n$CR$_1$R$_2$]X.[36] The QS parameter found for **10**·2PF_6 is the largest value found in the series of the bis(iron) dications **1** and **6**−**9**. It also compares well with the QS data found for the cumulenylidene iron complexes. For this series of compounds the variation of QS mainly depends on the anisotropic distribution of the electrons in the valence shell. An empiric linear relationship was observed for the distances between the iron and the α-carbon atoms $d_{(Fe-C\alpha)}$ and the quadruole splitting (eq 1).[36]

$$d_{(Fe-C\alpha)} = 0.34 \times QS + 1.41 \quad (1)$$

Application of eq 1 to the calculation of the Fe−Cα bond length in **10**·2PF_6 gives a distance of 1.80 Å, which compares very well with the same distance determined by X-ray diffraction (see above). These data are in full agreement with the diamagnetic character of complex **10**·2PF_6 and support a very strong cumulenic contribution for the electronic structure of the singlet ground state (structure B, Scheme 5). It is noteworthy that such a behavior is far from general, and this observation was unprecedented in the {[Fe]−C≡C−X−C≡C−[Fe]}$^{2+}$ compounds (X = aromatic rings or sp carbon atoms, [Fe] = Cp*(dppe)Fe) previously studied.[4]

The Mössbauer spectrum of the monocation **10**·TCNQ is also diagnostic of an original electronic structure for the MV complex. The presence of a unique doublet indicates that the two iron atoms are equivalent and **10**$^+$ is a detrapped class III MV complex, at least on the Mössbauer time scale. The IS and QS values are quite far from the average of those obtained for the neutral and the dicationic species. Indeed, the removal of the first electron from **10** induces a decrease of 81 and 92% for the IS and QS parameters, respectively, with respect to the total variation observed for the two-electron oxidation. It seems that most of the reorganization that occurs in the metal environment when compound **10** is transformed into **10**·2PF_6 is achieved after the first oxidation. Consequently, the iron atom in the mixed-valence complex **10**$^+$ should have a bonding closer to a cumulene-type structure than to an iron(III) alkyne. This result suggests that the first oxidation should be more carbon centered than the second oxidation. As averaged QS values were considered as a diagnostic of an important spin density on the metal centers in the MV state,[7,21,49−52,58] in the case of the cation **10**$^+$, it can be anticipated that the carbon bridge plays a decisive role in the delocalization of the unpaired electron. This is nicely confirmed by DFT calculations, which show that the unpaired electron in [**10-H**]$^+$ is spread out over the metal−spacer−metal backbone (see above). This is also in agreement with a larger gap between the SOMO and the rest of the occupied molecular orbitals in the anthracene series.

8. ESR Spectroscopy. The X-band ESR spectrum run at 77 K in a rigid glass ($CH_2Cl_2/C_2H_4Cl_2$, 1:1) for the complex **10**·PF_6 displays three features corresponding to the three components of the *g* tensor, as expected for d^5 low-spin iron(III) in pseudo-octahedral geometry.[4,59] The *g* values extracted from the spectra are collected in Table 8, together with some *g* values from the literature for MV complexes of the same Cp*(dppe)-Fe series. The g_{iso} ($g_{iso} = 1/3(g_1 + g_2 + g_3)$) tensor calculated for **10**·PF_6 corresponds to the smallest value found in this series. This suggests a larger carbon character of the SOMO for **10**·PF_6 than for all the other complexes of this series, which is confirmed theoretically (see above).

On the other hand, it was found for MV complexes of the bis-ferrocenium series that the anisotropy of the signal ($\Delta g = g_1 - g_3$) decreases as the rate of the

(53) Le Vanda, C.; Cowan, D. O.; Leitch, C.; Bechgaard, K. *J. Am. Chem. Soc.* **1974**, *96*, 6788.
(54) Le Vanda, C.; Bechgaard, K.; Cowan, D. O. *J. Org. Chem.* **1976**, *41*, 2700.
(55) Gütlich, P.; Link, R.; Trautwein, A. *Mössbauer Spectroscopy and Transition Metal Chemistry*; Springer-Verlag: Berlin, 1978; Vol. 3.
(56) Webb, R. J.; Geib, S. J.; Staley, D. L.; Rheingold, A. L.; Hendrickson, D. N. *J. Am. Chem. Soc.* **1990**, *112*, 5031.
(57) Varret, F.; Mariot, J.-P.; Hamon, J.-R.; Astruc, D. *Hyperfine Interact.* **1988**, *39*, 67.
(58) Hendrickson, D. N.; Oh, S. M.; Dong, T.-Y.; Kambara, T.; Cohn, M. J.; Moore, M. F. *Comments Inorg. Chem.* **1985**, *4*, 329.
(59) Rieger, P. H. *Coord. Chem. Rev.* **1994**, *135/136*, 203.

Scheme 5. Electronic Structure for 10^{2+}

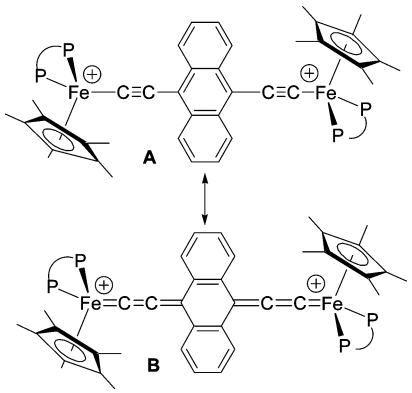

Table 8. ESR Data[a] for [Cp*(dppe)Fe−C≡C−X−C≡CFe(dppe)Cp*]$^+$

compd	g_1	g_2	g_3	g_{iso}	Δg	ref
1$^+$	2.079	2.089	2.139	2.102	0.060	7
6$^+$	2.054	1.999	2.054	2.108	0.109	13
7$^+$	2.031	2.043	2.199	2.091	0.168	46
8$^+$	2.170	1.975	2.032	2.505	0.530	33
9$^+$	2.053	2.006	2.039	2.113	0.107	21
10$^+$	2.018	2.035	2.105	2.052	0.083	this work

[a] At 77 K in $CH_2Cl_2/C_2H_4Cl_2$ (1:1) glass.

Table 9. UV−Vis Absorption Data of Complexes 10·NPF$_6$ and 7·NPF$_6$

compd	absorption λ/nm (10^3 ϵ/dm^3 mol^{-1} cm^{-1})
7	242 (87), 262 (63), 413 (25)
10	277 (24.2), 339 (17.6), 623 (30.0)
7·PF$_6$	246 (227), 268 (229), 546 (30), 702 (6)
10·PF$_6$	271 (25.5), 408 (8.1), 831 (15.0)
7·2PF$_6$	277 (199), 702 (55)
10·2PF$_6$	267 (76.0), 414 (13.3), 816 (50.3)

intramolecular electron transfer increases.[49,60] A similar observation was also made in the Cp*(dppe)Fe series, and the Δg tensor can be used to compare the rate of the electron transfer between different MV derivatives listed in Table 8.[21] The Δg values are significantly larger for the trapped MV **8**$^+$ than for the detrapped compounds **1**$^+$, **6**$^+$, **7**$^+$, and **9**$^+$ and the anthracene-containing complex **10**$^+$. This result clearly indicates that **10**$^+$ is a class III MV complex.

The ESR spectrum of **10**·2PF$_6$ recorded in a glass did not show any detectable signal. The spectrum of a pure powdered sample allowed the observation of a broad and very weak signal which could be attributed to minute amount of **10**·2PF$_6$ in the triplet state. However, the forbidden $\Delta m = \pm 2$ transition could not be detected. These observations are consistent with the NMR data and confirm that the molar fraction of compound **10**·2PF$_6$ in the triplet state is certainly not above 1%.

9. UV−Vis Spectroscopy. The UV−vis spectra of the complexes **10**·nPF$_6$ were recorded in CH_2Cl_2 and compared with those of the related complexes **7**·nPF$_6$ (Table 9). All spectra are dominated by intense bands below 400−420 nm, which can be attributed to an intraligand $\pi-\pi^*$ electronic transition. These bands are less intense and red shifted when the phenyl ring is replaced by anthracene. The neutral complex **10** presents an intense absorption band at 623 nm, which can be ascribed to a MLCT transition. A similar MLCT transition was observed for **7** at higher energy, 413 nm. Spectra of the dications **7**·2PF$_6$ and **10**·2PF$_6$ are quite similar, with LMCT bands at 702 and 816 nm, respectively. As for the neutral compounds, a band red shift is observed in the latter compound with respect to the former one.

The most interesting observation concerns the MV complexes. Complex **7**·PF$_6$ presents both MLCT and LMCT charge transfer bands at 546 and 702 nm, whereas **10**·PF$_6$ shows a unique band at 831 nm ascribed to a LMCT transition. Indeed, whereas the spectrum of **7**·PF$_6$ is intermediate between those of **7** and **7**·2PF$_6$, the spectra of **10**·PF$_6$ and **10**·2PF$_6$ are quite close (see Table 9). This suggests that the first one-electron oxidation induces an electronic structure reorganization more important in **10** with the anthracene group rather than in **7** with the phenyl ring. This conclusion is in full agreement with the Mössbauer data and can be rationalized by the DFT calculations.

10. NIR Spectroscopy. The spectrum of the neutral iron(II) complex **10** does not contain any absorptions in the NIR range. On the other hand, the spectrum of the dication **10**·2PF$_6$ displays weak absorptions centered at 5300 and 7490 cm^{-1} ($\epsilon \sim 700$ M^{-1} cm^{-1}, Table 10). The low-energy band is located at the same position as the forbidden ligand field (LF) transition generally observed for the Cp*(dppe)Fe(III) fragment. Indeed, similar absorption bands are invariably found for mononuclear and binuclear complexes containing this fragment.[4,20,61] Such a LF transition band was also observed for MV complexes having two weakly coupled Cp*(dppe)Fe$^{II/III}$ termini.[47] This spectroscopic behavior is consistent with two strongly antiferromagnetically coupled iron(III) centers. In this scheme, the HOMO−LUMO transition should be in the same energy range as the LF transition, but should have a larger transition moment. Moreover, the anthracene character being much larger in the LUMO than in the HOMO, this band can be regarded as a MLCT transition.

The NIR spectrum of the MV complex **10**·PF$_6$ shows an absorption band ca. 10 times more intense than the dication, which constitutes the signature of the intervalence charge transfer transition. This band presents a complex shape with a single well-defined maximum and shoulders (Figure 6). The spectra recorded in CH_2Cl_2 and CH_3CN are very similar. As the effect of the solvent on the IVCT transition is a function of the outer sphere Franck−Condon activation energy for the thermal electron transfer, it can be stated in the case of **10**·PF$_6$ that the intramolecular electron transfer is expected to be rapid on the time scale of solvent molecule reorganization ($\sim 10^{-12}$ s), and as a consequence, the solvation sphere of both redox centers is relatively symmetric.

As shown in Figure 6, the shape of the experimental band is complex and the analysis is not straightforward. Assuming that the IVCT bands should be approximated in terms of Gaussian band shapes, the spectrum was deconvoluted in the range 3300−9300 cm^{-1}. In the case of **10**·PF$_6$, the presence of a well-defined maximum and the distinct identification of two shoulders in the experimental spectrum facilitate the deconvolution process. The results show that three transitions con-

(60) Dong, T.-Y.; Sohel, C.-C.; Hwang, M.-Y.; Lee, T. Y.; Yeh, S.-K.; Wen, Y.-S. *Organometallics* **1992**, *11*, 573.

(61) Roué, S.; Lapinte, C. *J. Organomet. Chem.* **2005**, *690*, 594.

Table 10. Gaussian Analysis and Summary of the Electronic Spectral Data for the NIR Absorption Bands[a]

compd	band	ν_{max}	ϵ_{max} (M^{-1} cm^{-1})	$\Delta\nu_{1/2}^{exp}$ (cm^{-1})[b]	$\Delta\nu_{1/2}^{cal}$ (cm^{-1})[c]	V_{ab} [c] (cm^{-1})	ref
10^{+}	band A	4360	4200	1660	3170	2180	this work
		4340[d]	3900[d]	1660[d]		2170[d]	
	band B	5550	3300	2180	3580		
		5570[d]	2300[d]				
	band C	7700	2200	3360	4220		
		7470[d]	2200[d]				
10^{2+}	band A	5300	200				this work
	band B	7490	700				
6^{+}	band A	5030	25000	1500	3400	2515	13
	band B	6450	11700	3200	3900		
9^{+}	band A	5040	7900	1500	3400	2520	21
	band B	6450	6400	1200	3900		
	band C	10 000	12 000	5000	4800		

[a] In CH_2Cl_2, data in cm^{-1}. [b] Calculated from the Hush formula for a class II compound ($\Delta\nu_{1/2}^{calc} = (2310\nu_{max})^{1/2}$. [c] Calculated for a class III MV [V_{ab} (cm^{-1}) = ν_{max}/2]S. [d] In CH_3CN.

tribute to the absorption of **10**·PF_6 in the NIR. They are sufficiently good to allow an almost exact overlaying of the sum of the spectral components with the experimental spectra without filtration of the noise and residual vibration due to solvent subtraction. Table 10 summarizes spectral data extracted from the IVCT band shape analysis. The lowest energy band A, which constitutes the major component of the spectrum and corresponds to the superexchange, is approximately 2 times narrower than the value, which would be predicted by Hush's theory (see Table 10). Again, this is in agreement with the class III character of these MV compounds. Note that the position of the band does not depend on the polarity of the solvent, as expected for this type of complexes.

Comparison of the low-energy band observed for **10**·PF_6 and the related MV complexes **6**$^{+}$ and **9**$^{+}$ indicates that the absorption is less intense and located at lower energy in the case of the anthracene-containing compound. In addition, the calculated versus experimental full widths at half-height ($\Delta\nu_{1/2}$) ratio is also slightly smaller for this complex, in agreement with an electronic coupling approximately 10% smaller than in the **6**$^{+}$ and **9**$^{+}$ derivatives. Interestingly, the separation between the ground state and the excited state is significantly smaller in **10**·PF_6 (4360 cm^{-1}) than in the closely related MV **6**$^{+}$ and **9**$^{+}$ (~5040 cm^{-1}).

The presence of two other bands in the NIR range is not characteristic of the anthracene group. Indeed, three distinct absorption bands are also observed for the MV complex **6**$^{+}$, and the spectrum of the related derivatives **9**$^{+}$ shows two absorption bands, like many other MV systems. These bands, which are also characteristic of the MV state, should correspond to HOMO$-n$ to SOMO transitions.

Conclusion

The combined theoretical and experimental study on the family of complexes [Cp*(dppe)Fe$-$C≡C-9,10-ant-C≡C$-$FeCp*(dppe)][PF_6]$_n$ (n = 0, 1, 2) clearly establishes the good electronic communication existing between the iron centers across the bis(ethynyl)anthracene bridge, but the introduction of the anthracene fragment in the bridge of the bis(iron) complexes deeply modifies the nature of the interaction between the metal ends in **10**, **10**$^{+}$, and **10**$^{2+}$ with respect to their bis(iron) congeners **1** and **6**$-$**9**. The presence of anthracene makes the HOMO rather high in energy and separated by a significant energy gap from the rest of the occupied molecular orbitals. It favors also a rather low energy level of the LUMO for compound **10** with respect to the related bis(iron) complexes. The properties of the MV complex **10**$^{+}$ differ substantially from those of the related bis(iron) compounds. Indeed, the total metallic spin density is much smaller and the distribution is mainly found on the ethynyl fragments and on the *ipso* carbon atoms of the anthracene central ring. In the case of the dicationic compound **10**$^{2+}$ the singlet state is largely energetically favored and the triplet state lies above the singlet state by at least 1200 cm^{-1}. It is noteworthy that the properties of the series of complexes **10**$^{n+}$ are very close to those of the bis(ruthenium) derivatives [Cp*(dppe)Ru$-$C≡C$-$C≡C$-$Ru(dppe)] (**5**).[14] Interestingly, the replacement of iron by ruthenium in **1** or the introduction of the anthracene group in the $-C_4-$ bridge produces very similar effects. It is also important to emphasize that despite a iron$-$iron distance of ca. 12 Å and a large delocalization of the spin density on the carbon spacer, the radicals **10**$^{+}$ and **10**$^{2+}$ are thermally very stable.

Experimental Section

General Procedures. All the manipulations were carried out under an argon atmosphere using Schlenk techniques or in a Jacomex 532 drybox filled with nitrogen. Routine NMR spectra were recorded using a Bruker DPX 200 spectrometer. High-field NMR spectra experiments were performed on a multinuclear Bruker WB 300 instrument. Chemical shifts are given in parts per million relative to tetramethylsilane (TMS) for ^{1}H and ^{13}C NMR spectra and H_3PO_4 for ^{31}P NMR spectra. X-Band ESR spectra were recorded on a Bruker ESP-300E spectrometer. An Air Products LTD-3-110 liquid helium transfer system was attached for the low-temperature measurements. The ^{57}Fe Mössbauer spectra were obtained by using a constant acceleration spectrometer previously described with a 50 mCi ^{57}Co source in a Rh matrix. The sample temperature was controlled by an Oxford MD306 cryostat and an Oxford ITC4 temperature controller. Computer fitting of the Mössbauer data to Lorenzian line shapes was carried out with a previously reported computer program. The isomer shift values are reported with respect to iron foil at 298 K and are not corrected for the temperature-dependent second-order Doppler shift. The Mössbauer sample cell consists of a 2 cm diameter cylindrical plexiglass holder. Elemental analyses were performed at the Centre de Microanalyses du CNRS, Lyon-Solaise, France.

Synthesis of Cp*(dppe)Fe$-$C≡C-9,10-ant-C≡C$-$FeCp*-(dppe) (10). In a Schlenk tube wrapped with aluminum foil,

9,10-bis(trimethylsilylethynyl)anthracene (270 mg, 0.73 mmol) in 50 mL of methanol was stirred 10 h in the presence potassium carbonate (220 mg, 1.6 mmol, 2.2 equiv). Then Cp*(dppe)FeCl (1 g, 1.6 mmol, 2.2 equiv) and $NaBPh_4$ (547 mg, 1.6 mmol, 2.2 equiv) were added. After approximately 16 h of stirring, KOBu^t (190 mg, 2,2 equiv) was introduced. Stirring was maintained for 4 h before the solvent was removed. The residue was extracted with toluene (4 × 50 mL), and the solution was concentrated to ca. 5 mL. Addition of 80 mL of pentane allowed precipitation of a dark blue powder. The solid was washed with pentane (5 × 20 mL) and dried to give **10**. Yield: 940 mg (91%). Anal. Calcd for $C_{90}H_{86}P_4Fe_2 \cdot CH_2Cl_2$: C, 73.44; H, 5.96. Found: C, 73.57; H, 6.01. FT-IR (Nujol, cm^{-1}): 2010 (s, $\nu_{C\equiv C}$). ^{1}H NMR (200 MHz, C_6D_6): δ 8.58−8.42 (m, 4 H, ant); 8.20−8.00 (m, 8 H, Ph); 7.50−7.30 (m, 8 H, Ph); 7.20−7.00 (m, 28 H, Ph and ant); 3.01 (m, 4 H, CH_2); 2.02 (m, 4 H, CH_2); 1.65 (s, 30 H, $C_5(CH_3)_5$). ^{31}P NMR (81 MHz, C_6D_6): δ 102.1 (s, dppe). High-resolution MS (FAB): *m/z* 1402.4388 (calcd for $[C_{90}H_{86}P_4Fe_2]^+$ 1402.4379). Mössbauer (mm/s vs Fe, 80 K): IS = 0.262, QS = 1.958. X-ray-quality crystals of Cp*(dppe)Fe−C≡C-9,10-ant-C≡C−FeCp*(dppe)·CH_2Cl_2 were grown by slow diffusion of pentane into a saturated CH_2Cl_2 solution of the above compound.

Synthesis of [Cp*(dppe)Fe−C≡C-9,10-ant-C≡C−FeCp*(dppe)][PF$_6$] (10$^+$PF$_6^-$). To a mixture of complex **10** (200 mg, 0.143 mmol) and $[FeCp_2][PF_6]$ (64 mg, 0.136 mmol) was added 20 mL of THF. Overnight stirring at −80 °C gave a dark green solution, which was then concentrated to ca. 5 mL before 80 mL of Et_2O was added. The mixture was cooled at −60 °C to allow the precipitation of [Cp*(dppe)Fe−C≡C-9,10-ant-C≡C−FeCp*(dppe)][PF_6] as a black powder. Yield: 140 mg (67%). FT-IR (KBr, cm^{-1}): 1964 and 1901 (m, $\nu_{C\equiv C}$); 843 (m, ν_{P-F}). CV (CH_2Cl_2, 20 °C, 0.1 M *n*-Bu_4NPF_6, v = 0.1 V/s): $E^0{}_1$ = −0.386 V (ΔE_p = 0.075 V; $I_p{}^a/I_p{}^c$ = 1.0), $E^0{}_2$ = −0.034 V (ΔE_p = 0.066 V; $I_p{}^a/I_p{}^c$ = 1.0). UV−vis (CH_2Cl_2): λ_{max} (ϵ) 831 (15 000), 408 (8100), 271 (25 500), 257 (25 300). High-resolution MS (FAB): *m/z* 1402.4390 (calcd for $[C_{90}H_{86}P_4Fe_2]^+$ 1402.4379). ESR (CH_2Cl_2/$C_2H_4Cl_2$ 1:1, 77 K): g_x = 2.1050; g_y = 2.0350; g_z = 2.0175. NIR (CH_2Cl_2, cm^{-1}): (ϵ, $\Delta\nu_{1/2}$) 7700 (2230, 3560), 5550 (3310, 2780), 4360 (4150, 1660).

Synthesis of [Cp*(dppe)Fe−C≡C-9,10-ant-C≡C−FeCp*(dppe)][TCNQ] (10$^+$TCNQ$^-$). To a mixture of complex **10** (100 mg, 0.071 mmol) and TCNQ (15 mg, 0.071 mmol) was added 20 mL of THF. Stirring for 16 h at −80 °C gave a dark solution, which was then concentrated to approximately 5 mL before 80 mL of pentane was added. The mixture was cooled at −60 °C to allow the precipitation of **10**·TCNQ as a black powder. Yield: 70 mg (61%). FT-IR (Nujol, cm^{-1}): 2185, 2176, and 2151 (m, $\nu_C\equiv$N); 1957 and 1910 (m, $\nu_C\equiv$C). CV (CH_2Cl_2, 20 °C, 0.1 M *n*-Bu_4NPF_6, v = 0.1 V/s): $E^0{}_1$ = −0.392 V (ΔE_p = 0.080 V; $I_p{}^a/I_p{}^c$ = 1.0, 2 times more intense), $E^0{}_2$ = −0.050 V (ΔE_p = 0.060 V; $I_p{}^a/I_p{}^c$ = 1.0), $E^0{}_3$ = 0.184 V (ΔE_p = 0.068 V; $I_p{}^a/I_p{}^c$ = 1.0). UV−vis (CH_2Cl_2): λ_{max} (ϵ) 850 (23 400), 772 (14 800), 486 (9800), 402 (24 300), 259 (31 200), 232 (55 800). High-resolution MS (FAB): *m/z* 1402.4385 (calcd for $[C_{90}H_{86}P_4Fe_2]^+$ 1402.4379). Mössbauer (mm/s vs Fe): IS = 0.188 and QS = 1.206 (80 K); IS = 0.121 and QS = 1.134 (293 K). X-ray-quality crystals of [Cp*(dppe)Fe−C≡C-9,10-ant-C≡C−FeCp*(dppe)][TCNQ] were grown by slow diffusion of pentane into a saturated THF solution of the above compound.

Synthesis of [Cp*(dppe)Fe−C≡C-9,10-ant-C≡C−FeCp*(dppe)][PF$_6$]$_2$ (10^{2+}2PF$_6^-$). To a mixture of complex **10** (200 mg, 0.143 mmol) and $[FeCp_2][PF_6]$ (131 mg, 0.278 mmol) was added 30 mL of THF. Overnight stirring at −80 °C gave a green solution. The solution was then concentrated to approximately 5 mL, and 80 mL of Et_2O was added. The mixture was cooled at −60 °C to allow the precipitation of [Cp*(dppe)Fe−C≡C-9,10-Ant-C≡C−FeCp*(dppe)][PF_6]$_2$ as a green powder. Yield: 220 mg (91%). FT-IR (KBr, cm^{-1}): 839 (s, ν_{P-F}), 1943 and 1896 ($\nu_C\equiv$C). CV (CH_2Cl_2, 20 °C, 0.1 M *n*-Bu_4NPF_6, v = 0.1 V/s): $E^0{}_1$ = −0.376 V (ΔE_p = 0.078 V; $I_p{}^a/I_p{}^c$ = 1.0), $E^0{}_2$ = −0.026 V (ΔE_p = 0.070 V; $I_p{}^a/I_p{}^c$ = 1.0). UV−vis (CH_2Cl_2): λ_{max} (ϵ) 816 (50 300), 414 (13 300), 267 (76 000), 238 (72 700). ^{1}H NMR (200 MHz, CD_3COCD_3): δ 7.70−7.15 (m, 40 H, Ph); 6.95−6.80 (m, 8 H, ant); 4.43 (m, 4 H, CH_2); 3.38 (m, 4 H, CH_2); 1.46 (s, 30 H, $C_5(CH_3)_5$). ^{31}P NMR (81 MHz, CD_3COCD_3): δ 69.1 (s, dppe); −143.0 (sept, $^1J_{PF}$ = 707 Hz, PF_6^-). ^{13}C NMR (50 MHz, CD_3COCD_3): δ 271.2 (Fe−C$_\alpha$≡C); 144.4 (Fe−C≡C$_\beta$); 137.3−127.3 (Ar); 108.2 ($C_5(CH_3)_5$); 32.3 (m, CH_2); 10.4 ($C_5(CH_3)_5$). High-resolution MS (FAB): *m/z* 1547.4021 (calcd for $[C_{90}H_{86}P_4{}^{56}Fe_2{}^{2+},PF_6^-]^+$ 1547.4021). ESR (powder, 77 K): g = 2.03314 (weak signal, Δm_s = 2 was not observed). NIR (CH_2Cl_2, cm^{-1}): (ϵ, $\Delta\nu_{1/2}$) 9825 (1150, 2140), 7485 (740, 3000), 5300 (250, 2000). Mössbauer (mm/s vs Fe, 80 K): IS = 0.044; QS = 1.120. X-ray-quality crystals of [Cp*(dppe)Fe−C≡C-9,10-ant-C≡C−FeCp*(dppe)][PF_6]$_2$ were grown by slow diffusion of pentane into a saturated THF solution of the above compound.

Crystal Structures. Crystals of **10**·2CH_2Cl_2, **10**·TCNQ, and **10**·2PF_6 were glued to a glass fiber mounted on a four-circle Nonius Kappa CCD area-detector diffractometer. Intensity data sets were collected using Mo Kα radiation through the program COLLECT.[62] Correction for the Lorentz−polarization effect, peak integration, and background determination were carried out with the program DENZO.[63] Frame scaling and unit cell parameter refinement were performed with the program SCALEPACK.[63] Analytical absorption corrections were performed by modeling the crystal faces using NUMABS.[64] The structure was solved with the triclinic space group $P\bar{1}$. Iron and phosphorus atoms were located using the direct methods with the program SIR97.[65] The complete model was found from successive Fourier calculations using SHELXL-97.[66] All H atoms were generated and refined using the "riding" option available in SHELXL-97.

Computational Details. Density functional theory (DFT) calculations were carried out on model compounds [**1-H**]$^{n+}$, [**6-H**]$^{n+}$, [**7-H**]$^{n+}$, and [**10-H**]$^{n+}$ derived from the experimental structure data using the Amsterdam Density Functional (ADF) program,[67] developed by Baerends and co-workers.[68−72] Electron correlation was treated within the local density approximation (LDA) in the Vosko−Wilk−Nusair parametrization.[73] The nonlocal corrections of Becke and Perdew were added to the exchange and correlation energies, respectively.[74−76] The numerical integration procedure applied for the calculations was developed by te Velde et al.[77] The atom electronic configurations were described by a triple-ζ Slater-type orbital (STO) basis set for H 1s, C 2s and 2p, O 2s and 2p, P 3s and 3p augmented with a 3d single-ζ polarization for C, O, and P

(62) Nonius. *Kappa CCD Software;* Nonius BV: Delft, The Netherlands, 1999.
(63) Otwinowski, Z.; Minor, W. Processing of X-ray Diffraction Data Collected in Oscillation Mode. In *Methods in Enzymology, Macromolecular Crystallography*; Carter, C. W., Sweet, R. M., Ed.; Academic Press: New York, 1997; Vol. 276, Part A, p 307.
(64) Coppens, P. In *Crystallographic Computing*; Munksgaard Publishers: Copenhagen, 1970.
(65) Altomare, A.; Burla, M. C.; Camali, M.; Cascarano, G.; Giacovazzo, C.; Guagliardi, A.; Moliterni, A. G. G.; Polidori, G.; Spagna, R. *J. Appl. Crystallogr.* **1999**, *31*, 115.
(66) Sheldrick, G. M. *SHELX97. Program for Refinement of Crystal* Structures; University of Göttingen: Göttingen, Germany, 1997.
(67) 1996.
(68) Baerends, E. J.; Ellis, D. E.; Ros, P. *Chem. Phys.* **1973**, *2*, 41.
(69) Te Velde, G.; Baerends, E. J. *J. Comput. Phys.* **1992**, *99*, 84.
(70) Fonseca Guerra, C.; Snijders, J. G.; te Velde, G.; Baerends, E. J. *J. Theor. Chem. Acc.* **1998**, *99*, 391.
(71) Bickelhaupt, F. M.; Baerends, E. J. *J. Rev. Comput. Chem.* **2000**, *15*, 1.
(72) Te Velde, G.; Bickelhaupt, F. M.; van Gisbergen, S. J. A.; Fonseca Guerra, C.; Baerends, E. J.; Snijders, J. G.; Ziegler, T. J. *Comput. Chem.* **2001**, *22*, 931.
(73) Vosko, S. D.; Wilk, L.; Nusair, M. *Can. J. Chem.* **1990**, *58*, 1200.
(74) Becke, A. D. *J. Chem. Phys.* **1986**, *84*, 4524.
(75) Becke, A. D. *Phys. Rev.* **1988**, *A38*, 3098.
(76) Perdew, J. P. *Phys. Rev. B* **1986**, *33*, 8822.
(77) Perdew, J. P. *Phys. Rev.* **1986**, *B34*, 7406.

atoms and with a 2p single-ζ polarization for H atoms. A triple-ζ STO basis set was used for Fe 3d and 4s augmented with a single-ζ 4p polarization function for Fe. A frozen-core approximation was used to treat the core shells up to 1s for C and O, 2p for P, and 3p for Fe. Full geometry optimizations were carried out using the analytical gradient method implemented by Verluis and Ziegler.[78] Spin-unrestricted calculations were performed for all the open-shell systems. Representation of the molecular orbitals was done using MOLEKEL4.1.[79]

(78) Verluis, L.; Ziegler, T. *J. Chem. Phys.* **1988**, *88*, 322.
(79) Flükiger, P.; Lüthi, H. P.; Portmann, S.; Weber, J. *Swiss Center for Scientific Computing*; Manno, 2000−2001.

Acknowledgment. F.d.M. acknowledges the Ministry of Research and Education for a fellowship. K.C. and J.-F. H. thank the Pôle de Calcul Intentif de l'Ouest (PCIO) of the University of Rennes and the Institut de Développement et de Ressources en Informatique Scientifique (IDRIS-CNRS) of Orsay for computing facilities.

Supporting Information Available: The cif files for **10**, **10**·TCNQ, and **10**·2PF_6 are available free of charge at http://pubs.acs.org.

OM050403D